

A Disentangled Representation Learning Framework for Low-altitude Network Coverage Prediction

Xiaojie Li, Zhijie Cai, Nan Qi, *Senior Member, IEEE*, Chao Dong, *Senior Member, IEEE*, Guangxu Zhu, *Member, IEEE*, Haixia Ma, Qihui Wu, *Fellow, IEEE*, and Shi Jin, *Fellow, IEEE*

Abstract—The expansion of the low-altitude economy has underscored the significance of Low-Altitude Network Coverage (LANC) prediction for designing aerial corridors. While accurate LANC forecasting hinges on the antenna beam patterns of Base Stations (BSs), these patterns are typically proprietary and not readily accessible. Operational parameters of BSs, which inherently contain beam information, offer an opportunity for data-driven low-altitude coverage prediction. However, collecting extensive low-altitude road test data is cost-prohibitive, often yielding only sparse samples per BS. This scarcity results in two primary challenges: imbalanced feature sampling due to limited variability in high-dimensional operational parameters against the backdrop of substantial changes in low-dimensional sampling locations, and diminished generalizability stemming from insufficient data samples. To overcome these obstacles, we introduce a dual strategy comprising expert knowledge-based feature compression and disentangled representation learning. The former reduces feature space complexity by leveraging communications expertise, while the latter enhances model generalizability through the integration of propagation models and distinct subnetworks that capture and aggregate the semantic representations of latent features. Experimental evaluation confirms the efficacy of our framework, yielding a 7% reduction in error compared to the best baseline algorithm. Real-network validations further attest to its reliability, achieving practical prediction accuracy with MAE errors at the 5 dB level.

Index Terms—Low-altitude Network, Disentangled Representation Learning, RSRP, Coverage Map Prediction, AI for Communication.

I. INTRODUCTION

THE rapid development of the low-altitude economy, driven by emerging applications such as unmanned aerial vehicles (UAVs), low-altitude logistics, and aerial surveillance,

Xiaojie Li is with the National Mobile Communication Research Laboratory, Southeast University, Nanjing 210096, China, also with the College of Physics, Nanjing University of Aeronautics and Astronautics, Nanjing 210016, China, and also with the Shenzhen Research Institute of Big Data, The Chinese University of Hong Kong-Shenzhen, Guangdong 518172, China (e-mail: xiaojieli@nuaa.edu.cn).

Nan Qi, Chao Dong and Qihui Wu are with the Key Laboratory of Dynamic Cognitive System of Electromagnetic Spectrum Space, Ministry of Industry and Information Technology, Nanjing University of Aeronautics and Astronautics, Nanjing 210023, China (e-mail: nanqi.commun@gmail.com, dch@nuaa.edu.cn, and wuqihui@nuaa.edu.cn).

Zhijie Cai and Guangxu Zhu are with the Shenzhen Research Institute of Big Data, The Chinese University of Hong Kong-Shenzhen, Guangdong 518172, China (e-mail: zhijiecai@link.cuhk.edu.cn and gxzhu@sribd.cn).

Haixia Ma is with the College of Physics, Nanjing University of Aeronautics and Astronautics, Nanjing 210016, China (e-mail: mahaixia@nuaa.edu.cn).

Shi Jin is with the National Mobile Communications Research Laboratory and Frontiers Science Center for Mobile Information Communication and Security, Southeast University, Nanjing 210096, China (e-mail: jin shi@seu.edu.cn).

has generated an urgent demand for reliable and accurate Low-altitude Network Coverage (LANC) [1]. Ensuring seamless connectivity in such scenarios is crucial for enabling efficient network management [2]. As a result, the accurate modeling and prediction of LANC have become a prominent research focus.

Conventionally, existing 4G and 5G network coverage prediction research has focused on the coverage prediction of terrestrial networks. For instance, in certain typical scenarios [3], such as indoor or outdoor, rural or urban settings, empirical models [4] or stochastic geometric models [5]–[8] have been employed. However, these approaches lack the capability to describe specific environments in detail [9], thereby limiting accuracy. To address this, ray tracing [10]–[12] has been utilized in conjunction with local map modeling to simulate coverage in specific environments. Nevertheless, the challenges of accurately modeling environments and the high computational complexity remain significant hurdles for ray tracing technology [13], [14]. Moreover, advanced deep learning methods have also been applied to coverage prediction [15]–[19]. Most of these methods [15], [16] have achieved high prediction accuracy based on simulated datasets, and some works based on real-world data [17]–[19] have demonstrated the potential of this approach.

With the burgeoning development of the low-altitude economy, researchers have redirected their attention to LANC prediction [2]. In contrast to terrestrial networks, low-altitude networks will be planned in airspace with fewer buildings, leading to the predominance of received signals from direct paths. Consequently, the actual LANC is largely influenced by the multi-beam capabilities of base stations (BSs) and the collaborative effect of multiple BSs [20]. This shifts the focus from conventional environmental scattering to base station antenna configurations and beamforming patterns. Moreover, many terrestrial models treat the vertical dimension as negligible, making them unsuitable for the three-dimensional nature of low-altitude networks. The traditional terrestrial solutions, which are primarily designed for ground-level environments, are inadequate for addressing these challenges. As a result, there is a clear need for novel approaches specifically tailored to the unique requirements of low-altitude networks.

In response to this need, many recent studies have attempted to explore the prediction of LANC. However, most of these studies primarily concentrate on 3-dimensional (3D) coverage interpolation for individual regions, i.e., 3D radio map reconstruction. These approaches seek to enhance reconstruction accuracy by incorporating factors such as trajectory optimization

[21] and channel shadowing [22], relying on sparse sampling within the area of interest and lacking the capability for cross-regional generalization. Such cross-regional generalization is critical for practical network planning and deployment, as it enables reliable coverage prediction in previously unseen areas without the need for extensive on-site measurements. Additionally, some efforts have been made towards theoretical modeling of ground-to-air channels within low-altitude networks [23]–[25]. Nevertheless, a limited understanding of real-world BS models, i.e., the actual beam setting, has constrained their performance. In summary, there is still a notable gap in research that considers the actual multi-beam effects of BSs and possesses the capability for generalizing LANC prediction across various regions.

In reality, if we could access the multi-beam directionality diagrams of BS antennas [26] in cellular networks, it would be feasible to achieve generalization across BSs and even across regions. However, the direct representation of BS antenna multi-beam directionality diagrams is proprietary information of the equipment manufacturers, making it difficult to access. Fortunately, BS configuration parameters implicitly contain beam-related information [27], including the Active Antenna Unit (AAU) type, number of antenna channels, coverage scenario, and factors influencing the beam direction, such as down tilt and azimuth. By effectively leveraging this information, it is possible to infer the impact of multi-beam gain from BSs.

Given the increasing availability of BS operational data and the high cost of large-scale measurements, leveraging learning-based methods for predicting LANC using sparse low-altitude coverage data becomes feasible. However, during road tests, UAVs primarily capture RSRP from the serving base station within a limited coverage area. Despite traveling several kilometers, the data collected often reflects only a small subset of base stations, typically no more than 30, with each contributing data from a specific region. This results in an imbalanced distribution of data, as high-dimensional base station parameters are sparsely sampled across the entire coverage space, while low-dimensional locations exhibit greater variation. Additionally, the high cost of data collection in early low-altitude economies further limits the compilation of extensive LANC data [28], restricting the generalization capability of learning models. Ultimately, feature imbalance and data scarcity pose significant challenges to developing models with robust accuracy and generalization.

As shown in Fig. 1, we have designed a disentangled representation learning framework to overcome the proposed obstacles. On one hand, embedding expert knowledge, such as signal propagation models, can enhance model generalization with limited samples. By leveraging this expertise for feature compression, we obtain a more balanced and compressed feature space, which helps mitigate generalization challenges. On the other hand, disentangled representation learning [29], which focuses on learning the latent representations of distinct independent factors, has demonstrated its effectiveness in improving model interpretability, controllability, robustness, and generalization across several fields, including computer vision, natural language processing, and data mining. Inspired by this approach, we categorize the compressed features based

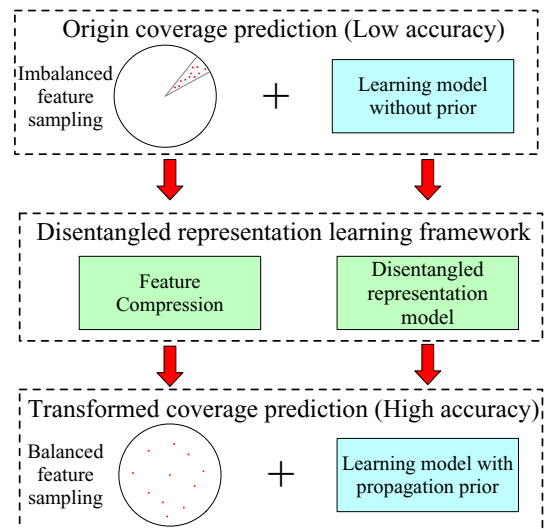


Fig. 1: Disentangled representation learning framework.

on different independent aspects [30] of signal propagation, which enables the dissection of various components affecting signal propagation, thereby enhancing prediction accuracy and generalization.

In summary, we propose a disentangled representation learning framework for the prediction of LANC based on BS operational parameters. Our contributions can be summarized as follows:

- **Feature Compression Based on Expert Knowledge:** As part of the proposed framework, we leverage expert knowledge in the field of communications to compress features of BS operational parameters and sparse measurement data in the original feature space. This feature compression effectively addresses the issue of feature imbalance caused by imbalanced sampling across the feature space, providing a solid foundation for accurate and efficient LANC prediction.
- **Model-guided Disentangled Representation Network:** Our framework incorporates a disentangled representation network guided by the signal propagation model, which enhances both generalizability and interpretability. The theoretical analysis demonstrates that the proposed network, while using fewer parameters, maintains comparable learning capabilities to traditional deep neural networks (DNNs) in LANC prediction tasks. This reduction in model complexity ensures improved generalization performance, particularly under limited data conditions.
- **Experiments with Real-world Network Data:** We validated the proposed framework through real-world low-altitude data collection and network training conducted in Nanchang, Jiangxi Province, China. Ablation studies demonstrate our framework reduces the mean absolute error (MAE) by approximately 20% compared to traditional DNNs. Furthermore, our method outperforms the best baseline algorithm with a 7% reduction in error. In practical LANC prediction of an unknown area, the framework achieves a measured MAE error at the 5 dB level, demonstrating its reliability and applicability in

real-world scenarios.

The remainder of this work is organized as follows: Section II introduces the system model and problem formulation. Following this, the proposed disentangled representation learning framework is detailed in Section III. Section IV provides a theoretical analysis of the proposed framework. Empirical evaluations, including ablation studies, comparisons with existing algorithms on real-world datasets, and further performance validation, are presented in Section V. Finally, Section VI concludes the paper.

II. SYSTEM MODEL AND PROBLEM FORMULATION

A. BS and Its Operational Parameters

In scenarios such as BS pre-planning or where low-altitude sparse data collection is absent, predicting low-altitude coverage based on operational parameters becomes a prevalent approach. For such a BS of interest, the operational parameters crucially linked to coverage can be systematically categorized based on their roles in determining coverage as follows:

- **Absolute Location Attributes:** The parameters of *longitude*, *latitude*, and *antenna height* are pivotal in pinpointing the absolute position of the BSs. These locational attributes provide a foundational understanding of the BS's placement relative to the coverage area.
- **Static Characteristics of the Antenna Beam:** The *AAU type*, *number of channels*, *coverage scenario*, and *carrier frequency* are integral in defining the static characteristics of the antenna beam. Specifically, the AAU type dictates the availability of channels at the BS, while the configuration of coverage scenarios allows for the emission of signals aligned with the beam antenna patterns tailored to each scenario at a corresponding carrier frequency. These characteristics collectively delineate the static characteristics of the antenna beam.
- **Orientation Characteristics of the Antenna Beam:** The orientation characteristics of the antenna beam are uniquely determined by the *horizontal azimuth*, *beam azimuth*, *mechanical down tilt*, and *digital down tilt*. Adjusting these angles enables precise control over the antenna's orientation, affecting coverage in both horizontal and vertical planes.
- **Additive Signal Strength Features:** The *total transmission power* and *bandwidth* are categorized as additive signal strength features. Given a carrier frequency, the total bandwidth collectively establishes the effective utilization bandwidth for the antenna beams emitted by the BS. The antenna beams' transmission power is derived from the total transmission power.

For ease of description, the aforementioned categories and the included operational parameters are defined in Table I.

B. Low-altitude Coverage for Area of Interest

To further explore the LANC provided by the BS, consider a nearby area with dimensions $U \times W \times V$ m³, corresponding to its longitudinal, latitudinal, and altitudinal extents. This area can be subdivided into N cubes, where $N = N_U \times$

TABLE I
Category of Operational Parameters and Corresponding Mathematical Expression

Category	Vector	Parameters	Scalar
Absolute Location Attributes	$\mathbf{x}^{(L)}$	Longitude	$x_1^{(L)}$
		Latitude	$x_2^{(L)}$
		Antenna Height	$x_3^{(L)}$
Static Characteristics of the Antenna Beam	$\mathbf{x}^{(S)}$	AAU Type	$x_1^{(S)}$
		Num of Channels	$x_2^{(S)}$
		Coverage Scenario	$x_3^{(S)}$
		Carrier Frequency	$x_4^{(S)}$
Orientation Characteristics of the Antenna Beam	$\mathbf{x}^{(O)}$	Horizontal Azimuth	$x_1^{(O)}$
		Beam Azimuth	$x_2^{(O)}$
		Mechanical Down Tilt	$x_3^{(O)}$
		Digital Down Tilt	$x_4^{(O)}$
Additive Signal Strength Features	$\mathbf{x}^{(A)}$	Total Transmission Power	$x_1^{(A)}$
		Bandwidth	$x_2^{(A)}$

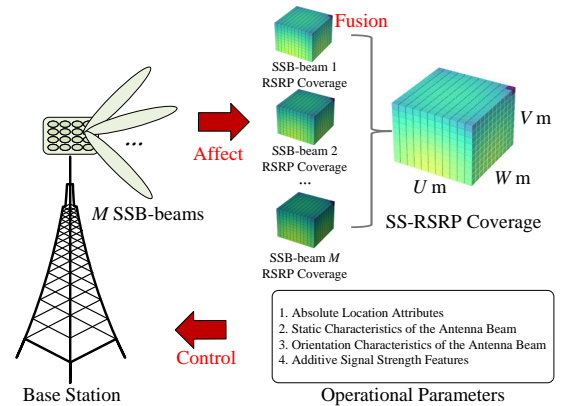


Fig. 2: The process of low-altitude coverage prediction based on operational parameters.

$N_W \times N_V$ and N_U , N_W , and N_V represent the counts of discretization along the longitude, latitude, and altitude axes, respectively. The set of cubes can thus be defined as $\mathbf{R} = \{1, \dots, r_n, \dots, r_N\}$. For cube r_n , the absolute position vector can be defined as $\mathbf{x}_n^{(R)} = [x_{n,1}^{(R)}, x_{n,2}^{(R)}, x_{n,3}^{(R)}]^T$, where $x_{n,1}^{(R)}$, $x_{n,2}^{(R)}$ and $x_{n,3}^{(R)}$ are longitude, latitude, and altitude, respectively. Furthermore, the absolute position array for all cubes is defined as $\mathbf{X}^{(R)} = [\mathbf{x}_1^{(R)}, \dots, \mathbf{x}_n^{(R)}, \dots, \mathbf{x}_N^{(R)}] \in \mathbb{R}^{3 \times N}$.

Determined by the AAU type, the BS will emit M beams. For any given cube n , M Synchronization-Signaling-Block-RSRP (SSB-RSRP) measurements can be obtained, along with a maximum SSB-RSRP, denoted as SS-RSRP. These measurements can be represented as $\mathbf{p}_n = [p_{n,0}, p_{n,1}, \dots, p_{n,m}, \dots, p_{n,M}]^T \in \mathbb{R}^{M \times 1}$, where $p_{n,0}$ is the SS-RSRP for the n -th cube, and $p_{n,m}$ represents the m -th SSB-RSRP for the n -th cube. Consequently, the coverage for all cubes within the area can be expressed as $\mathbf{P} = [\mathbf{p}_1, \dots, \mathbf{p}_n, \dots, \mathbf{p}_N] \in \mathbb{R}^{M \times N}$.

C. Problem Formulation

As shown in Fig. 2, the objective of the study is to identify a learning machine, denoted as g , capable of predicting multi-beam RSRP coverage at the cube level, based on given operational parameters. For this task, the absolute position features of the cubes and the BS should be transformed into relative features. Specifically, for any cube r_n , the relative position feature is defined as

$$\Delta \mathbf{x}_n^{(R)} = \mathbf{x}_n^{(R)} - \mathbf{x}^{(L)}. \quad (1)$$

Thus, at cube r_n , the prediction of multi-beam RSRP \mathbf{p}_n can be denoted as¹

$$\hat{\mathbf{p}}_n = g(\mathbf{x}^{(S)}, \mathbf{x}^{(O)}, \mathbf{x}^{(A)}, \Delta \mathbf{x}_n^{(R)}). \quad (2)$$

For the whole area, the prediction of \mathbf{P} can be denoted as $\hat{\mathbf{P}} = [\hat{\mathbf{p}}_1, \dots, \hat{\mathbf{p}}_N] \in \mathbb{R}^{M \times N}$. Finally, the problem of coverage prediction can be formulated as

$$\min_g L(\mathbf{P}, \hat{\mathbf{P}}), \quad (3)$$

where L denotes a loss function that quantifies the discrepancy between $\hat{\mathbf{P}}$ and \mathbf{P} . The primary aim of the learning machine g is to minimize this loss, thereby enabling precise prediction of the RSRP coverage performance at each point within the area of interest, based on the operational parameters.

To tackle Problem (3), an intuitive approach involves leveraging sparse measurement samples from additional BSs and employing conventional supervised learning frameworks to develop regression models, such as Random Forest. However, this approach faces significant challenges due to imbalanced feature sampling. Specifically, with just a 2° discretization for variables like the horizontal azimuth, beam azimuth, mechanical down tilt, and digital down tilt, the parameter search space expands to the magnitude of 10^8 (i.e., $360/2 \times 360/2 \times 180/2 \times 180/2$ permutations). UAV-based low-altitude road measurements over a 3km \times 3km area, however, engage only a few dozen BSs (around 50 combinations of operational parameters). This poses significant challenges for the generalization capability of conventional approaches. To address these challenges, we propose a disentangled representation learning framework that enhances the prediction and generalization performance for Eq. (3) through feature compression based on expert knowledge and the design of a disentangled representation neural network.

III. DISENTANGLED REPRESENTATION LEARNING FRAMEWORK

A. Expert-knowledge-based Feature Compressing

In Section II, we preliminarily categorized the sample features based on expert knowledge into $\mathbf{x}^{(S)}$, $\mathbf{x}^{(O)}$, $\mathbf{x}^{(A)}$,

and $\Delta \mathbf{x}_n^{(R)}$. It is important to note that when considering $\{\mathbf{x}^{(S)}, \mathbf{x}^{(O)}, \mathbf{x}^{(A)}, \Delta \mathbf{x}_n^{(R)}\}$ as a complete set of sample features, the variation among different samples is primarily concentrated in the three-dimensional $\Delta \mathbf{x}_n^{(R)}$, while the ten-dimensional variation of $\{\mathbf{x}^{(S)}, \mathbf{x}^{(O)}, \mathbf{x}^{(A)}\}$ is relatively minor. This directly leads to sample imbalance. In fact, only $\mathbf{x}^{(S)}$ is solely related to the type of BS and exhibits less variation. $\mathbf{x}^{(O)}$ can be combined with $\Delta \mathbf{x}_n^{(R)}$ to calculate the relative angle of the target cube with respect to the antenna panel's facing direction. Specifically, the horizontal and vertical angles of cube r_n relative to the BS's true north direction are first calculated using $\Delta \mathbf{x}_n^{(R)}$, i.e.,

$$\theta_n^{(H)} = \arctan 2(\Delta x_{n,1}^{(R)}, \Delta x_{n,2}^{(R)}), \quad (4)$$

$$\theta_n^{(V)} = \arctan(\Delta x_{n,3}^{(R)} / \sqrt{\Delta x_{n,1}^{(R)2} + \Delta x_{n,2}^{(R)2}}), \quad (5)$$

where $\theta_n^{(H)}$ and $\theta_n^{(V)}$ are the horizontal and vertical angles of cube r_n relative to the BS's true north direction, respectively. The elements $\Delta x_{n,1}^{(R)}$, $\Delta x_{n,2}^{(R)}$, and $\Delta x_{n,3}^{(R)}$ represent the first, second, and third components of $\Delta \mathbf{x}_n^{(R)}$, respectively. These components signify the differences in longitude, latitude, and altitude dimensions between cube r_n and the considered BS. Eq. (4) returns the horizontal relative angle of r_n with respect to the true north direction of the considered BS, with a range of $[-\pi, \pi]$ (in radians).

It is noted that the angles of the elements within $\mathbf{x}^{(O)}$ are relative to the BS's true north direction. Consequently, the relative angle of cube n with respect to the antenna panel's normal direction (denoted as $\Delta \theta_n^{(H)}$ for horizontal and $\Delta \theta_n^{(V)}$ for vertical) can be computed as follows:

$$\Delta \theta_n^{(H)} = \theta_n^{(H)} - x_1^{(O)} - x_2^{(O)}, \quad (6)$$

$$\Delta \theta_n^{(V)} = \theta_n^{(V)} - x_3^{(O)} - x_4^{(O)}. \quad (7)$$

Since $\Delta \theta_n^{(H)}$ and $\Delta \theta_n^{(V)}$ already characterize the relative angular relationship between cube n and the antenna panel, the angular information contained in $\Delta \mathbf{x}_n^{(R)}$ is redundant. Given the orthogonality of the polar coordinate system, it is only necessary to extract the distance feature from $\Delta \mathbf{x}_n^{(R)}$, i.e.,

$$D_n = \sqrt{\Delta x_{n,1}^{(R)2} + \Delta x_{n,2}^{(R)2} + \Delta x_{n,3}^{(R)2}} \quad (8)$$

Now, we have transform the imbalanced variation of $\Delta \mathbf{x}_n^{(R)}$ and $\mathbf{x}^{(O)}$ into that of $\Delta \theta_n^{(H)}$, $\Delta \theta_n^{(V)}$ and D_n along with n . Next, we will decouple the influence of $\mathbf{x}^{(A)}$ based on the signal propagation model. Generally speaking, the received SSB-RSRP, $p_{n,m}$, at location r_n for the m th beam can be described as

$$p_{n,m} = p^{(T)} + G_{n,m}^{(T)} + PL_{n,m} + G^{(R)}. \quad (9)$$

Here, $p^{(T)}$ represents the transmission power of the SSB signal, $G_{n,m}^{(T)}$ denotes the directional gain of the BS for the

¹The prediction model in Eq. (2) does not account for the shadowing effects caused by the surrounding environment of the BS deployment. This omission is considered reasonable for low-altitude coverage predictions at heights of 50 meters or above. At such altitudes, the coverage performance is primarily influenced by beamforming and the attenuation of line-of-sight (LOS) links. The potential gains resulting from environmental factors can be discussed in future work.

²Theoretically, variations in the digital down tilt of a BS are not entirely equivalent to changes in the mechanical down tilt. For practical applications, it is acceptable to consider the total down tilt of a BS as the sum of the digital down tilt and the mechanical down tilt.

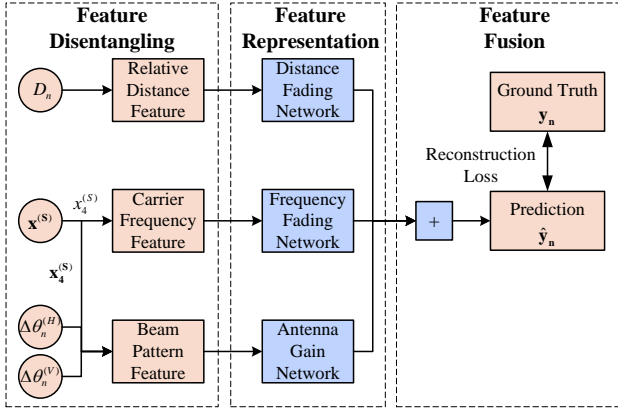


Fig. 3: The design of our disentangled representation network, where distance fading, frequency fading, and antenna gain networks can be a simple MLP for feature representation, respectively.

m th beam at grid r_n , and $G^{(R)}$ is the gain of the receiver antenna. $PL_{n,m}$ is the path fading between cube r_n and corresponding beam m .³ Given that subsequent experiments are conducted using the same single-antenna UAV, without loss of generality, we simplify the receiver antenna to an omnidirectional antenna.

Theoretically, $p^{(T)}$ can be obtained from $x_1^{(A)} - 10 \log_{10} x_2^{(A)}$. However, due to the actual SSB signal bandwidth utilization not being 100% and its susceptibility to the BS's carrier frequency and bandwidth, represented by σ , the actual $p^{(T)}$ is given by

$$p^{(T)} = x_1^{(A)} - 10 \log_{10} x_2^{(A)} - 10 \log_{10}(\sigma). \quad (10)$$

Thus, the impact of $\mathbf{x}^{(A)}$ has been decoupled. Let $y_{n,m}$ denote $p_{n,m} - p^{(T)}$. Then set $\mathbf{y}_n = [y_{n,0}, y_{n,1}, \dots, y_{n,m}, \dots, y_{n,M}]^T \in \mathbb{R}^{M \times 1}$. The prediction task (2) can be transformed into

$$\hat{\mathbf{y}}_n = g(\mathbf{x}^{(S)}, \Delta\theta_n^{(H)}, \Delta\theta_n^{(V)}, D_n). \quad (11)$$

By incorporating expert knowledge, the transformation of the prediction task has addressed the issue of imbalanced feature variation. Simultaneously, it significantly reduces the dimensionality of the input variables, thereby ensuring an enhancement in coverage prediction performance. Next, we will introduce the corresponding disentangled representation network design.

B. Disentangled-network-based Feature Representation

To predict LANC for a target BS, a neural network is initially trained using road test data and the sparse collections from other available BSs. This network is designed to execute the prediction task from input to output, as specified in Eq. (11). Firstly, we will introduce the core motivation behind our network design. According to Eq. (9), the prediction target \mathbf{y}_n

³In the context of LANC, different beams may follow distinct paths, leading to varied path fading.

is primarily composed of a linear addition of two parts: $PL_{n,m}$ and $G_{n,m}^{(T)}$ (where $G^{(R)}$ is considered as an omnidirectional antenna and can be omitted for simplicity). Drawing on literature [31], $PL_{n,m}$ (considering the characteristics of low-altitude networks, shadowing is not taken into account here) can be further expressed as

$$PL_{n,m} = \alpha \log_{10} D_n + \beta \log_{10} x_4^{(S)}. \quad (12)$$

However, the assumptions of this log model form may limit data fitting performance. Therefore, we adopt a relaxed expression for \mathbf{y}_n , that is:

$$\mathbf{y}_n = f_1(\Delta\theta_n^{(H)}, \Delta\theta_n^{(V)}, \mathbf{x}_4^{(S)}) + f_2(D_n) + f_3(x_4^{(S)}). \quad (13)$$

Here, $\mathbf{x}_4^{(S)} = [x_1^{(S)}, x_2^{(S)}, x_3^{(S)}]^T$. $f_1(\cdot)$, $f_2(\cdot)$, and $f_3(\cdot)$ are obtained through fitting with neural networks.

Overall, as illustrated in Fig. 3, the design of the neural network comprises three main components: 1) Feature Disentangle, 2) Feature Representation, and 3) Feature Fusion. In the following, we will detail each of these components.

1) *Feature Disentangle*: According to Eq. (13), the inputs for the entire network are set to include $\Delta\theta_n^{(H)}$, $\Delta\theta_n^{(V)}$, $\mathbf{x}_4^{(S)}$, D_n , and $x_4^{(S)}$, where $\{\Delta\theta_n^{(H)}, \Delta\theta_n^{(V)}, \mathbf{x}_4^{(S)}\}$, D_n , and $x_4^{(S)}$ are fed into different neural networks for semantic extraction.

2) *Feature Representation*: Here, the relative distance, carrier frequency, and beam pattern features are respectively fed into the distance fading, frequency fading, and antenna gain networks to learn semantic representations. All networks utilize Multi-Layer Perceptron (MLP) architectures.

Specifically, for the distance fading and frequency fading networks, due to the assumption made in Eq. (9) that, given r_n , signals from different beams exhibit different path fading, both networks output a semantic vector of dimension $M+1$. For the antenna gain network, given a BS, its $x_2^{(S)}$ and $x_3^{(S)}$ are fixed, but the sparse sampling positions affect $\Delta\theta_n^{(H)}$ and $\Delta\theta_n^{(V)}$. Therefore, the antenna gain network can learn the semantics of gain across different relative angles in the beam antenna pattern for a given station. Moreover, as the BS changes, $x_2^{(S)}$ and $x_3^{(S)}$ will also change, thereby facilitating the antenna gain network's learning of gain variations across different stations. Given that the antenna patterns vary across beams, the antenna gain network outputs a vector of dimension $M+1$.

3) *Feature Fusion*: According to Eq. (13), the outputs from different networks can be summed to obtain the predicted $\hat{\mathbf{y}}_n$, which is then compared with the actual sparse measurements \mathbf{y}_n to compute the reconstruction loss. Without loss of generality, we employ MSELoss as the reconstruction loss, defined as

$$L(\mathbf{y}_n, \hat{\mathbf{y}}_n) = \frac{1}{M+1} \|\mathbf{y}_n - \hat{\mathbf{y}}_n\|_2^2, \quad (14)$$

where $\|\cdot\|_2$ denotes the L2 norm of a vector. It is noteworthy that the outputs of the three networks are added directly. Consequently, the partial derivative of the loss with respect to each network's output is 1. This characteristic encourages each network to continually learn and adjust its weights to minimize the reconstruction loss.

IV. THEORETICAL ANALYSIS OF DISENTANGLED REPRESENTATION LEARNING FRAMEWORK

In this section, the proposed disentangled representation learning framework will be explained. Initially, evidence for the designed feature disentangling and representation processes will be presented.

A. An Explanation on the Efficacy of Feature Disentangling and Representation

It is noted that in Fig. 3, $\{\Delta\theta_n^{(H)}, \Delta\theta_n^{(V)}, \mathbf{x}_4^{(S)}\}$, $\{D_n\}$, and $\{x_4^{(S)}\}$ are independent features and we use a single representation for them respectively. This setting can result in lower overfitting risk. We will next give a more general proof.

1) Definitions:

Definition 1 (Decomposable data). Consider we are given K sets of signal vectors as a set of realizations of a corresponding independent random variable, e.g., $\{\mathbf{x}_i^k\}_{i \in [N]} \sim X^k, k \in [K]$. A dataset is formed by concatenating signal vectors from different sets, e.g., $\mathbf{x}_i = [\mathbf{x}_i^{1T}, \dots, \mathbf{x}_i^{KT}]^T$.

Definition 2 (Full model). A full model $P_{\mathbf{w}}(Z|X)$ parameterized by \mathbf{w} is used to code each \mathbf{x}_i into some feature \mathbf{z}_i , where $\mathbf{w} \in \mathcal{W} \subset \mathbb{R}^d$, where \mathcal{W} is the biggest subset allowed by the model structure, d is the number of parameters contained in the model.

Definition 3 (Constrained model). A constrained model is a full model but with $\mathbf{w} \in \mathcal{W}_c \subseteq \mathcal{W}$, where \mathcal{W}_c is a constrained subset allowed by the model structure.

Remark 1. Without abuse of notation, we denote by \mathbb{R} the set of real numbers. For example, for a common MLP, we can regard that $\mathcal{W} = \mathbb{R}^d$. Since modern deep neural network models are large in the number of parameters, the model is often over-parameterized and biased to the seen training data, resulting in a phenomenon known as overfitting. A method to mitigate the effect is to narrow the search space based on some a priori knowledge. For example, by knowing that some of the parameters in the model are redundant, [32] proposed DropOut to stochastically choose some dimensions of \mathbf{w} and constrain the domain of that dimension to $\{0\}$.

Definition 4 (Learning capability). Considering the generalization requirements of LANC prediction, we adopt the generalization error [33] as a metric to characterize the model's learning capability. Given a model parameter \mathbf{w} , a set of training data $\{\mathbf{x}_i\}$, and a loss function $\ell(\mathbf{x}, \mathbf{w})$, the learning capability is defined as

$$\text{gen}(\mathbf{w}, \{\mathbf{x}_i\}) := \left| \mathbb{E}_{\bar{\mathbf{x}} \sim X} [\ell(\bar{\mathbf{x}}, \mathbf{w})] - \mathbb{E}_{\mathbf{x} \in \{\mathbf{x}_i\}} [\ell(\mathbf{x}, \mathbf{w})] \right|. \quad (15)$$

Remark 2. The learning capability characterizes the gap between the model's performance on training samples and that on test samples, unseen by the model but assumed to follow the same distribution. A model demonstrating strong generalization will exhibit reduced learning capability disparity.

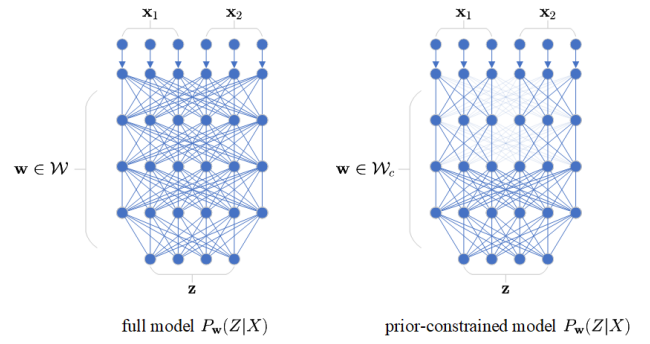


Fig. 4: Full model and prior constrained model.

2) *Decomposing model for comparable learning capability:* We try to establish that our proposed prior-constrained model structure can maintain a comparable learning capability to traditional DNNs. From an angle of deep learning practitioners, knowing how \mathbf{x} is independently composed of $[\mathbf{x}^{1T}, \dots, \mathbf{x}^{KT}]$, we propose to design dedicated *model heads* for each of the components as shown in Fig. 4. Then, to make use of the full data, we aggregate the output of the heads as the final feature by concatenation. This procedure is equivalent to a constrained model. To see this, take a toy example of the linear layer in a full model, transforming a vector of d dimensions into one of d_1 dimensions. The weight of this layer can be viewed as a matrix $\mathbf{w} \in \mathbb{R}^{d \times d_1}$. To gain a corresponding constrained model, some dimension of \mathbf{w} can be constrained to $\{0\}$.

Lemma 1 (Learning capability bounded by mutual information [34]). When the loss function ℓ is subgaussian, we have

$$\text{gen}(\mathbf{w}, X) \leq \sqrt{2\sigma^2 I(\mathbf{w}; X)} \quad (16)$$

over the randomness of the stochastic learning algorithm, where X denotes the training set as a random variable.

Remark 3. Subgaussianity is an easy qualification since a bounded function is always subgaussian.

Definition 5 (Equivalent indicator). C is a binary random variable, takes value 1 if a $\mathbf{w} \in \mathcal{W}_c$ else 0.

Proposition 1 (Comparable learning capability of constrained model). The constrained model exhibits an upper bound on learning capability that is not greater than its corresponding full model, reflecting a desirable reduction conducive to improved generalization.

Proof. We form a Markov chain $X \leftrightarrow \mathbf{w} \leftrightarrow C$. By Kolmogorov's identity, we have

$$I(X, C; \mathbf{w}) = I(X; \mathbf{w}) + \underbrace{I(X; C|\mathbf{w})}_{=0, \text{Markovian}} \quad (17)$$

$$= I(X; C) + I(X; \mathbf{w}|C). \quad (18)$$

Since mutual information I is nonnegative, we will always have $I(X; \mathbf{w}|C) \leq I(X; \mathbf{w})$, i.e., the learning capability bound of the constrained model isn't more than that of the full model. \square

Proposition 2 (Lower overfitting risk of the constrained model). *The constrained model demonstrates a lower risk of overfitting compared to its corresponding full model.*

Proof. Based on Proposition 1, the constrained model achieves comparable learning capability. Moreover, the constrained model is characterized by a reduced number of learnable parameters, which inherently limits its capacity to overfit noise or spurious patterns in the training data. This reduction in model complexity effectively lowers the risk of overfitting. \square

B. An Explanation on the Efficacy of Feature Fusion

Based on the explanation in subsection IV-A, we understand that under deterministic prior knowledge, it is possible to artificially set certain parts of the MLP to zero, thereby ensuring a lower overfitting risk. According to Eq. (13), we know that the semantics represented by three separate parts can be summed to obtain the predicted RSRP. To embed this piece of knowledge into the model, we only need to change the feature fusion part in Fig. 4 from an MLP to an addition operation (setting specific parameters in the MLP to zero can achieve this addition). Therefore, by artificially setting parameters to zero once again, we modify the model following Eq. (13), maintaining the comparable learning capability.

V. EXPERIMENTAL RESULT

A. Dataset

To evaluate the performance of the proposed method, initial low-altitude road tests were conducted across three distinct areas within Nanchang City, Jiangxi Province. For these tests, a UAV equipped with a road test terminal flew at varying altitudes (150m, 300m, 500m). The terminal was capable of receiving multiple SSB-Beams' RSRP and PCI values from the downlink of the serving cell BSs. Utilizing the PCI values, the terminals identified and matched the nearest BS with the corresponding PCI within the area. The samples collected from each region during the tests are presented in Table II.

B. Experiment Setting

For the task of predicting coverage for BSs that have not been field-tested or are pending deployment, we have partitioned the entire dataset by binding each BS with its corresponding sparse samples. We then randomly divided the dataset centered around the BSs, as suggested in [35]. This approach ensures physical isolation between different BSs, preventing data leakage due to the consideration of relative positional features as input.

In subsequent experiments, we define s as the BS sampling rate, which represents the proportion of the dataset allocated to the training set. The validation set is consistently set to occupy 10% of the dataset, resulting in the test set comprising $90\% - s$ of the dataset. Given the significant impact of dataset partitioning on experimental outcomes, we conduct 20 experiments for each training set proportion. These experiments maintain a fixed proportion but vary based on different random seeds, ranging from 0 to 19. To assess the performance of different algorithms, we employ the common coverage metric, i.e., MAE, on the test set.

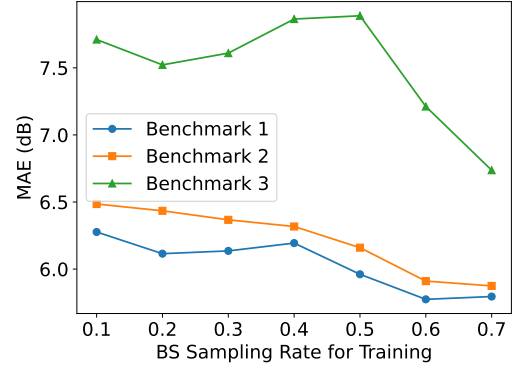


Fig. 5: Average MAE for different algorithms across 20 random splits (random seeds 0-19) as a function of the BS sampling rate in ablation experiments.

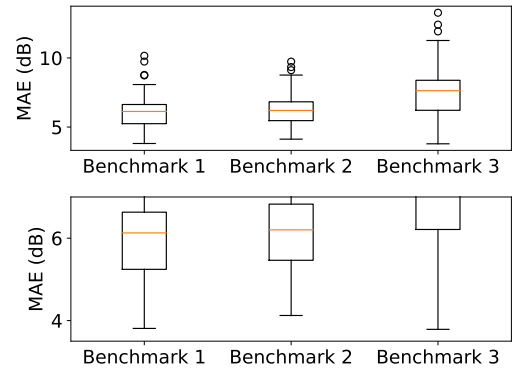


Fig. 6: Boxplot of MAE performance for different algorithms across 20 random splits at sampling rates of [10%, 20%, 30%, 40%, 50%, 60%, 70%], totally 140 MAE data points per algorithm.

C. Ablation Study Result

1) *Network Structure Comparison:* To validate the advanced nature of the proposed network structure, we established three benchmarks listed in Table III for ablation studies. In all benchmarks, the number of neurons in the hidden layers is set to 256, with the ReLU function serving as the activation function. For all benchmarks, the learning rate is set to 0.001, with a maximum of 100 epochs. Early stopping is implemented, terminating training when the loss on either the training or validation set decreases by no more than 1% over ten consecutive epochs. For benchmark 1, the hidden layer counts for distance fading, frequency fading, and antenna gain networks are all 5. In contrast, benchmarks 2 and 3 feature 6 hidden layers. Compared to the benchmark proposed in this paper, benchmark 2 utilizes decoupled features as inputs and employs an MLP to perform predictions as depicted in Eq. (11). Conversely, benchmark 3 employs original features as inputs and uses an MLP to execute predictions according to Eq. (2).

To demonstrate the effectiveness of the disentangled feature and network modules, we initially conducted exper-

TABLE II
Simple Description of Dataset

Area Index	Longitude	Latitude	Length (m)	Width (m)	Height (m)	Total Sample Number	Corresponding BS Number
1	115.69	28.61	4006	4273	150,300,500	43919	33
2	115.73	28.71	1501	1262	150,300,500	25322	50
3	115.79	28.68	1862	1134	150,300,500	24598	59

TABLE III
Benchmarks for Ablation Study

Benchmark	Backbone	Compressed Feature	Disentangled Network
1	Proposed	✓	✓
2	MLP	✓	✓
3	MLP	✓	✓

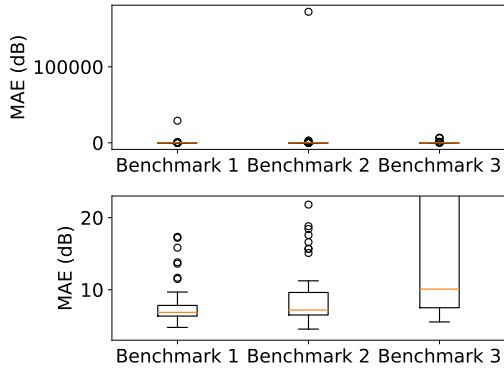


Fig. 7: Boxplot of MAE performance for different algorithms across 20 random splits at sampling rates of [1%, 2%, 3%, 4%, 5%, 6%], totally 120 MAE data points per algorithm.

iments with 20 different dataset splits at sampling rates of [10%, 20%, 30%, 40%, 50%, 60%, 70%]. For each sampling rate, we plotted the average MAE across benchmarks 1-3, as illustrated in Fig. 5. It is observable that the prediction errors for benchmarks 3, 2, and 1 progressively decrease, which validates the efficacy of the module design proposed in this study. Furthermore, as the sampling rate increases, the trends of the MAE curves for all three methods are consistently aligned, with overall performance gradually improving. This indicates that with an increase in training dataset size, the algorithms can learn a more precise distribution of the original dataset.

2) *Network Structure Robustness*: To demonstrate the robustness of the proposed algorithm, we visualized the boxplots of different algorithms during ablation experiments, as shown in Fig. 6. The different subplots within the figure visualize varying ranges of the Y-axis. Compared to benchmark 2, the proposed algorithm exhibits a lower mean and smaller fluctuation range. However, benchmark 2 achieves a lower maximum MAE, which may be attributed to the accidentality of outliers. The significantly higher MAE of benchmark 3 underscores the importance of feature compression design.

TABLE IV

Alternative Input for Different Networks in Proposed Method, where Networks 1, 2 and 3 for Distance Fading, Frequency Fading, and Antenna Gain Networks, Respectively

Model	Network 1	Network 2	Network 3
Proposed	D_n	$x_4^{(S)}$	$\Delta\theta_n^{(H)}, \Delta\theta_n^{(V)}, \mathbf{x}_4^{(S)}$
Wrong Model 1	D_n	$\Delta\theta_n^{(H)}$	$x_4^{(S)}, \Delta\theta_n^{(V)}, \mathbf{x}_4^{(S)}$
Wrong Model 2	$\Delta\theta_n^{(H)}$	$x_4^{(S)}$	$D_n, \Delta\theta_n^{(V)}, \mathbf{x}_4^{(S)}$
Wrong Model 3	$\Delta\theta_n^{(H)}$	$\Delta\theta_n^{(V)}$	$D_n, x_4^{(S)}, \mathbf{x}_4^{(S)}$

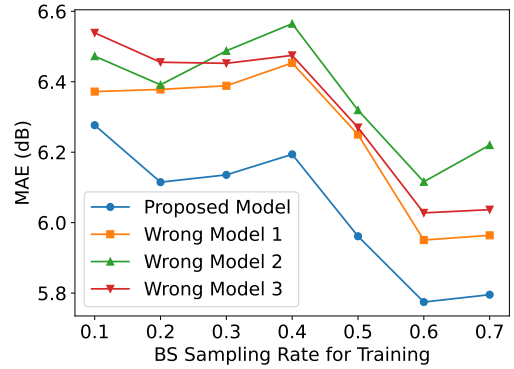


Fig. 8: Average MAE for different model knowledge across 20 random splits (random seeds 0-19) as a function of the BS sampling rate.

Moreover, we conducted experiments with 20 random splits at low sampling rates of [1%, 2%, 3%, 4%, 5%, 6%] to simulate early stages of low-altitude network planning with markedly insufficient training data, as well as scenarios where the algorithm is applied across different cities or operators with few matched AAU types between the test and training sets. As illustrated in Fig. 7, it is evident that even at such low training set proportions, the proposed method still achieves acceptable MAE performance (less than 7.5 dB) on the test set for 75% of the cases, significantly outperforming other algorithms. This further highlights the model's robustness in scenarios with low data availability.

3) *Importance of Right Model Knowledge*: Based on the model described in Eq. (13), we understand that the sets $\{\Delta\theta_n^{(H)}, \Delta\theta_n^{(V)}, \mathbf{x}_4^{(S)}\}$, $\{D_n\}$, and $\{x_4^{(S)}\}$ should be fed into distinct neural networks for learning representations. To investigate the impact of model correctness on learning performance, we considered alternative input combinations for the distance fading, frequency fading, and antenna gain networks,

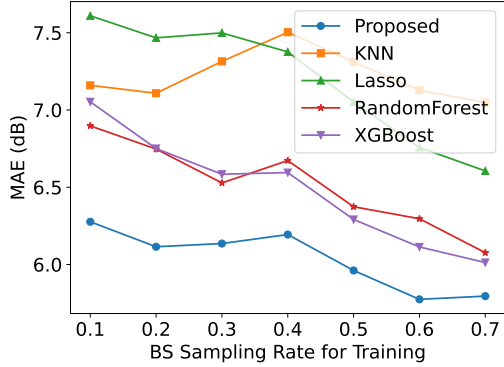


Fig. 9: Average MAE for different algorithms across 20 random splits (random seeds 0-19) as a function of the BS sampling rate in ablation experiments.

TABLE V
BS Operational Parameters Setting

Parameters	BS 1	BS 2
Antenna Height	39.86m	38.0m
Coverage Scenario	SCENARIO_0	SCENARIO_21
Num of Channels	32T32R	64T64R
AAU Type	AAU5336e	AAU5636
Mechanical down tilt	9.72°	0°
Horizontal Azimuth	359°	240°
Relative SSB Power	0dB	2.01dB

which are denoted as wrong models 1, 2, and 3, respectively, as shown in Table IV. Furthermore, we have illustrated the MAE performance of these models in Fig. 8. It can be observed that the proposed model has an MAE error of less than other wrong models at all BS sampling rates. Compared with the best wrong model 1, the MAE of the proposed model decreases by about 0.2 dB on average. The observed superior performance of the proposed model highlights the importance of proper model knowledge guidance. Notably, wrong model 1 outperforms wrong models 2 and 3 slightly, which may be attributed to model 1 maintaining a separate network for the D_n input, assigning it a greater weight in impact on coverage prediction.

It is important to note that not all possible combinations of model inputs were tested in this study. However, the experiments conducted sufficiently demonstrate the significance of correct knowledge in the considered model, Eq. (13), for coverage prediction. It is worth mentioning that beyond the models of this discussion, the channel propagation model, Eq. (13), may have more accurate prior knowledge structures, potentially leading to better feature preprocessing and combined representations. This could result in improved prediction performance, involving more precise channel propagation modeling, high-quality data-driven learning, and their trade-offs.

D. Algorithm Comparison

In addition to the ablation study, the proposed method was compared with several traditional machine learning methods,

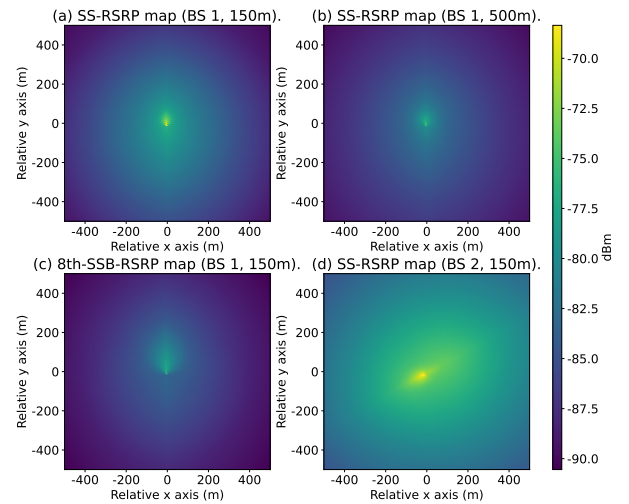


Fig. 10: The prediction coverage visualization results for different operational parameters under different conditions.

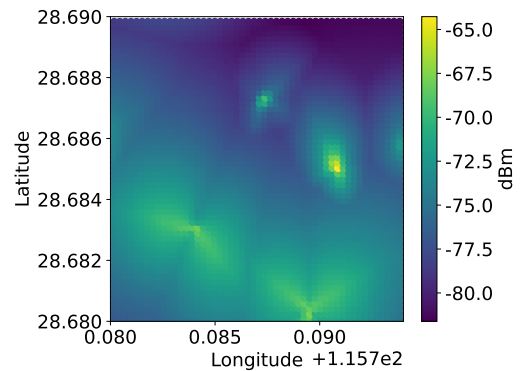


Fig. 11: SS-RSRP coverage map visualization in Xinyue Lake before operation parameters optimization.

including KNN [36] (with the number of neighbors set to 50), Lasso [37] (with a regularization strength of 1), Random Forest [38] (with 100 trees), and XGBoost [39] (using mean squared error as the objective). As shown in Fig. 9, the MAE of different algorithms was plotted against varying BS sampling rates. The results indicate that the proposed method consistently outperforms traditional methods across various BS sampling rates, achieving an average MAE improvement of approximately 0.5 dB. This further demonstrates the superiority of the proposed method.

E. Applications and Visualizations

Beyond basic experimental evaluations, which include ablation studies and algorithmic comparisons with machine learning methods, we have also conducted extensive application validations on additional real-world datasets to demonstrate the efficacy of the proposed method.

1) *Low-altitude Coverage Prediction for An Individual BS*: The effective prediction of low-altitude coverage for individual base stations constitutes a crucial foundation for network coverage. To illustrate the capability of the method

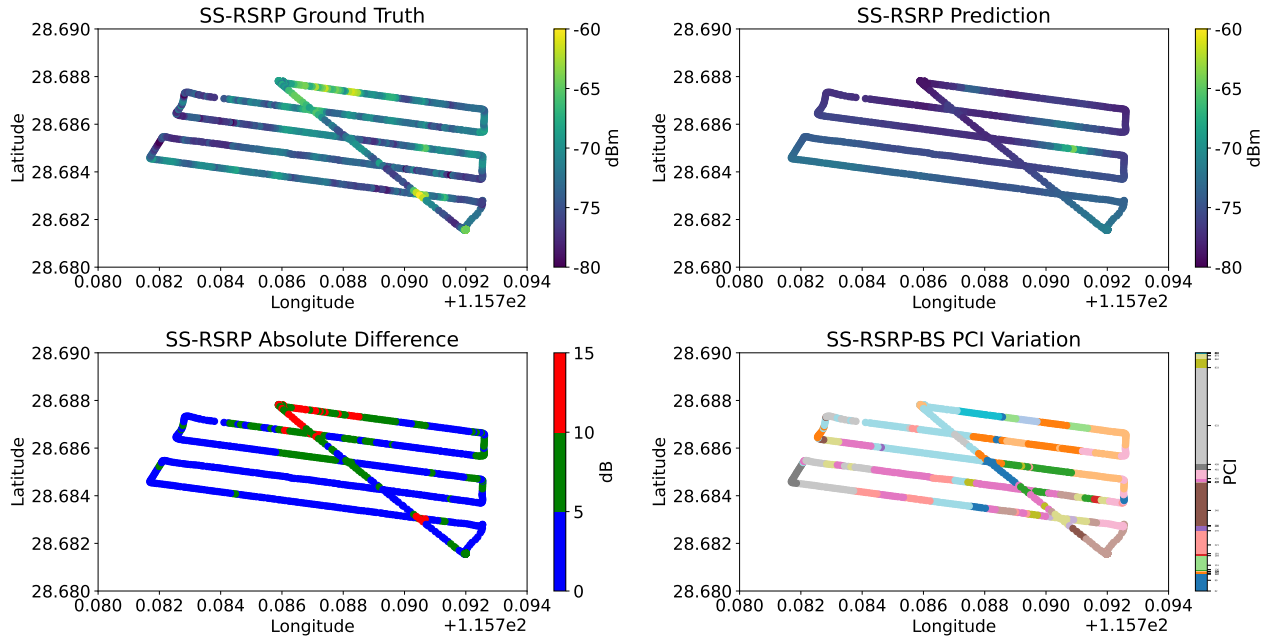


Fig. 12: Comparison of predicted and actual coverage at sampling locations in Xinyue Lake before operational parameters optimization (top left: actual SS-RSRP coverage at sampling locations, top right: predicted SS-RSRP coverage at sampling locations, bottom left: absolute difference between actual and predicted SS-RSRP at sampling locations, bottom right: UAV PCI switching during flight).

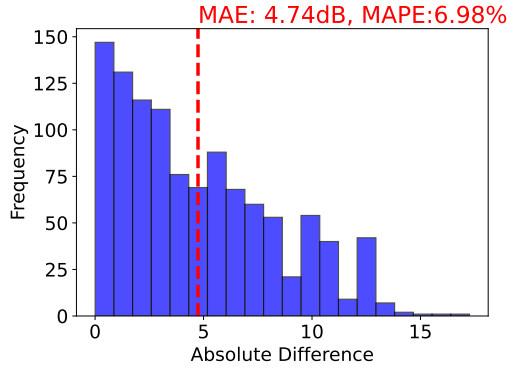


Fig. 13: The distribution of truth-prediction absolute error for all samples in Xinyue Lake before operation parameters optimization.

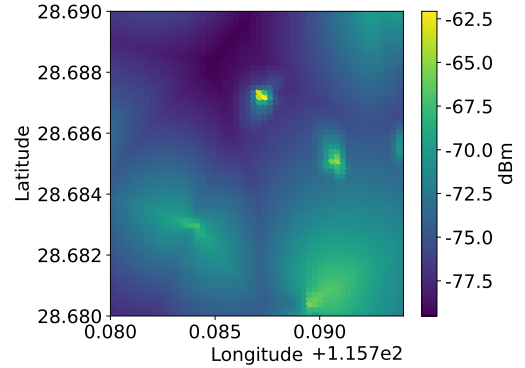


Fig. 14: SS-RSRP coverage map visualization in Xinyue Lake after operation parameters optimization.

in predicting the coverage of a single base station, we have visualized the coverage prediction of the proposed method under different operational parameters as shown in Table V⁴. Given the extremely limited sample size for individual base stations, it is challenging to quantitatively assess the prediction performance. Therefore, we provide a brief analysis of different coverage prediction results in conjunction with the operational parameters.

⁴We only show the different operational parameters. The relative SSB power in Table V is calculated as shown in Eq. (10). In addition, SCENARIO_0 represents a common ground-based wide beam configuration, whereas SCENARIO_21 is configured for aerial beamforming.

From the comparisons in Fig. 10(a) with 10(b) and 10(c), it is evident that the predicted SS-RSRP coverage is better than the predicted 8th-SSB-RSRP coverage. The coverage at a height of 500 meters is slightly weaker than that at 150 meters. From the comparisons in Fig. 10(a) with 10(d), the proposed method effectively captures changes in the horizontal angles of BS parameters and demonstrates better overall low-altitude coverage performance under aerial beam configurations.

2) *Multi-BS Coverage Prediction before Operational Parameters Optimization*: To identify low-altitude coverage holes, it is often necessary to predict the joint coverage of multiple BSs within a specific area. To achieve this, the proposed method first predicts the coverage of individual BSs.

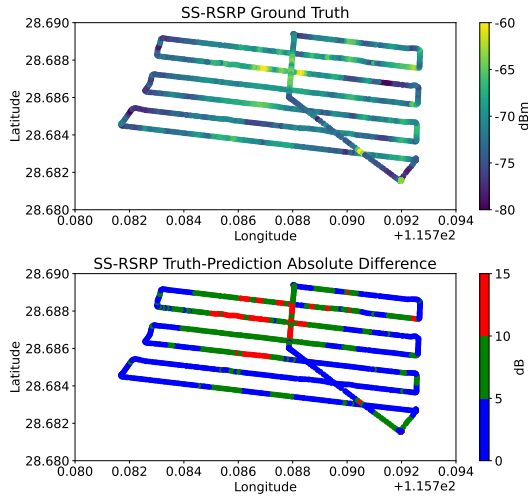


Fig. 15: Comparison of predicted and actual coverage at sampling locations in Xinyue Lake after operational parameters optimization (top: actual SS-RSRP coverage at sampling locations, bottom: absolute difference between actual and predicted SS-RSRP at sampling locations).

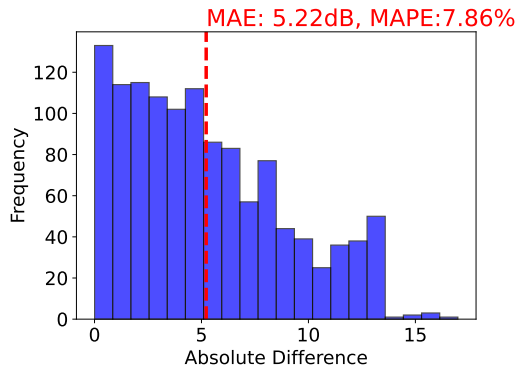


Fig. 16: The distribution of truth-prediction absolute error for all samples in Xinyue Lake after operation parameters optimization.

Then, the coverage predictions of multiple BSs are combined and rasterized, with the maximum predicted RSRP in each grid selected as the predicted SS-RSRP coverage for that grid. Using the trained model, we selected an area in the Xinyue Lake region of Jiangxi Province, involving 40 BSs. For each BS, the coverage at a height of 120 meters and a radius of 2000 meters (with a resolution of $10\text{m} \times 10\text{m}$) was predicted and combined. To ensure no data leakage, we removed all samples in the training set with longitude in $[115.78, 115.794]$ and latitude in $[28.68, 28.69]$ and trained the proposed model again, as the training set contained some low-altitude UAV measurement samples from the Xinyue Lake region. The visualization results can be shown in Fig. 11.

To evaluate the accuracy of the predictions, additional low-altitude measurements were conducted at a height of 120 meters. The predicted results were sampled at the same locations as the test points and compared with the new measurement

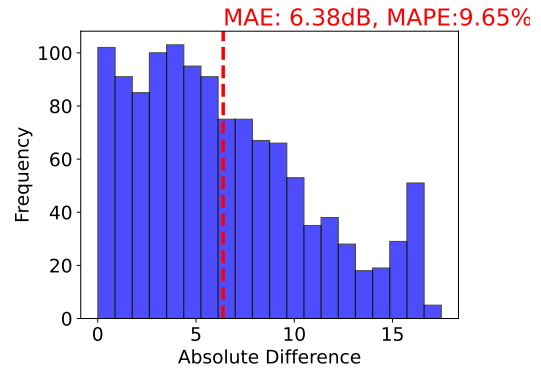


Fig. 17: The distribution of truth-prediction absolute error for all samples in Xinyue Lake after operation parameters optimization (if the prediction is sampled from surface coverage in Fig. 11).

results. The visualization results are shown in Fig. 12. It can be observed that the predicted SS-RSRP closely matches the measured RSRP, with the absolute difference between predicted and measured SS-RSRP values being less than 5 dB for most points. Based on the UAV measurement data of PCI changes for connected BSs, it is evident that larger prediction errors primarily occur at sampling points where BS handovers take place. These sudden handovers introduce prediction errors, which is reasonable. To reduce such errors, future works of coverage modeling and prediction could be incorporated by actual BS handover parameters and cell relationships.

To provide a more precise prediction error, we visualized the distribution of the absolute differences between predicted and measured SS-RSRP values across sampling locations in Fig. 13. The results show over 90% of the sampling have an error of less than 8 dB, and the MAE across all sampling locations is 4.74 dB. This further demonstrates the accuracy and practicality of the proposed method.

3) *Multi-BS Coverage Prediction after Operational Parameters Optimization*: To enhance the quality of low-altitude coverage in the area, we optimized the operational parameters of 20 BSs in the region following the method described in [26]. Based on the optimized parameters, the coverage at a height of 120 meters was re-predicted and re-measured⁵, as shown in Fig. 14 and 15. Moreover, the coverage prediction error distribution of all samples was visualized in Fig. 16, demonstrating that the proposed algorithm maintained excellent MAE performance. To more effectively demonstrate the algorithm's effectiveness in adjusting network operational parameters for coverage prediction, we sampled based on the surface coverage in Fig. 11 and calculated the MAE for the adjusted sampling points, as illustrated in Fig. 17. A comparison between Fig. 16 and Fig. 17 reveals that the accuracy of surface coverage prediction based on adjusted operational parameters outperforms the accuracy before adjustment, showing an approximate 18% performance improvement. This indicates the proposed algorithm's sensitivity to parameter adjustments,

⁵We take a new round of low-altitude trajectory collection at 120 meters.

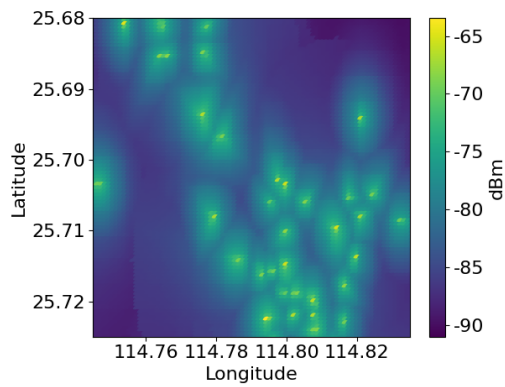


Fig. 18: SS-RSRP coverage map visualization in Ganzhou.

allowing for highly accurate coverage evaluation after network optimization.

4) *Multi-BS Coverage Prediction in Ganzhou without AAU Type of BSs*: When predicting low-altitude coverage across different operators, cities, or equipment manufacturers, the AAU type of the BSs to be predicted is often unknown during model training. To verify the performance of the proposed method in this case, we selected BSs along a low-altitude flight path in Ganzhou, Jiangxi Province, as the subjects for prediction. Given that the BSs in Ganzhou are all manufactured by ZTE, while those in the training data are from Huawei, all the AAU types of the BSs to be predicted are considered as a new category. Consequently, we excluded the AAU type feature $x_1^{(S)}$ from the input features and retrained a model using the training set. By inputting the operational parameters of the BSs (a total of 60 BSs) along the flight path, we predicted the low-altitude coverage at 150 meters altitude. Specifically, we predicted the RSRP for each of the 8 beams of every BS, followed by stacking and rasterization, with the maximum predicted RSRP in a grid defined as the grid SS-RSRP. The predicted surface coverage is shown in Fig. 18. Further sampling of the surface coverage, as illustrated in Fig. 19, reveals that the majority of the sampling points along the flight path have a predicted error of less than 5 dB. To quantify the error more accurately, as shown in Fig. 20, we visualized the distribution of the absolute differences between predicted SS-RSRP and real sampled SS-RSRP. The method proposed in this study achieved an MAE of 6.26 dB and a MAPE of 7.96%, demonstrating the reliability of the method and its transferability across different operator scenarios.

VI. CONCLUSION

This research has made significant strides in addressing the intricate challenge of low-altitude network coverage (LANC) prediction, a cornerstone for the burgeoning aerial economy. Recognizing the impediment faced by equipment manufacturers in accessing BS antenna beam patterns, we innovatively leveraged BS operational parameters for the prediction of LANC, adopting a data-driven model that marks a substantial advancement over traditional approaches.

Our research has introduced two pioneering techniques: feature compression based on expert knowledge and a model-

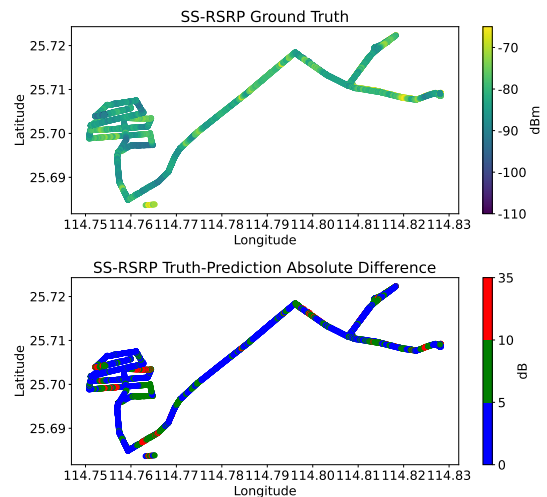


Fig. 19: Comparison of predicted and actual coverage at sampling locations in Ganzhou (top: actual SS-RSRP coverage at sampling locations, bottom: the absolute difference between actual and predicted SS-RSRP at sampling locations).

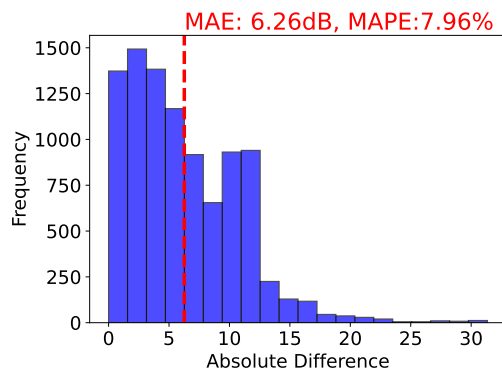


Fig. 20: The distribution of truth-prediction error for all samples in Ganzhou after operation parameters optimization.

guided disentangled representation network. The former not only achieves data compression but also addresses the issue of feature imbalance, while the latter, by integrating a signal propagation model, mitigates reliance on extensive data and reduces the risk of overfitting. Both of the techniques have demonstrated their efficacy in our experimental validation based on real-world data. These methodologies significantly enhance the accuracy of low-altitude coverage prediction.

However, we acknowledge the limitations of our study, particularly the insufficient consideration of environmental obstructions affecting signal propagation in low-altitude networks, and the opportunity to integrate more precise propagation models into our neural network architecture. Future endeavors will focus on exploiting large-scale data and large language models to refine LANC predictions. We also aim to incorporate detailed environmental data and BS beamforming patterns into our models, thus improving the precision and resilience of LANC.

REFERENCES

- [1] Y. Jiang, X. Li, G. Zhu, H. Li, J. Deng, K. Han, C. Shen, Q. Shi, and R. Zhang, "Integrated sensing and communication for low altitude economy: Opportunities and challenges," *IEEE Commun. Mag.*, pp. 1–7, 2025.
- [2] M. Rihan, D. Wübben, A. Bhattacharya, M. Petrova, X. Yuan, A. Schmeink, A. Fellan, S. Tayade, M. Zarour, D. Lindenschmitt, H. Schotten, and A. Dekorsy, "Unified 3D Networks: Architecture, Challenges, Recent Results, and Future Opportunities," *IEEE Open J. Veh. Technol.*, vol. 6, pp. 170–201, 2025.
- [3] C. Huang, R. He, B. Ai, A. F. Molisch, B. K. Lau, K. Haneda, B. Liu, C.-X. Wang, M. Yang, C. Oestges *et al.*, "Artificial Intelligence Enabled Radio Propagation for Communications—Part II: Scenario Identification and Channel Modeling," *IEEE Trans. Antennas Propag.*, vol. 70, no. 6, pp. 3955–3969, 2022.
- [4] V. Abhayawardhana, I. Wassell, D. Crosby, M. Sellars, and M. Brown, "Comparison of Empirical Propagation Path Loss Models for Fixed Wireless Access Systems," in *Proc. IEEE Veh. Technol. Conf.*, vol. 1, Stockholm, Sweden, Dec. 2005, p. 73–77.
- [5] J. Bian, C.-X. Wang, X. Gao, X. You, and M. Zhang, "A General 3D Non-Stationary Wireless Channel Model for 5G and Beyond," *IEEE Trans. Wireless Commun.*, pp. 3211–3224, May 2021.
- [6] C.-X. Wang, J. Bian, J. Sun, W. Zhang, and M. Zhang, "A Survey of 5G Channel Measurements and Models," *IEEE Commun. Surv. Tutorials*, vol. 20, no. 4, pp. 3142–3168, 2018.
- [7] I. Winner, "WINNER II channel models," *IST-4-027756 WINNER II, D. I. 1. 2 VI. 2*, 2007.
- [8] D. Baum, J. Hansen, G. Galdo, M. Milojevic, J. Salo, and P. Kyosti, "An Interim Channel Model for Beyond-3g Systems Extending the 3GPP Spatial Channel Model (SCM)," in *Proc. IEEE Veh. Technol. Conf.*, vol. 5, Stockholm, Sweden, Dec. 2005, pp. 3132–3136.
- [9] Y. Zeng, J. Chen, J. Xu, D. Wu, X. Xu, S. Jin, X. Gao, D. Gesbert, S. Cui, and R. Zhang, "A Tutorial on Environment-Aware Communications via Channel Knowledge Map for 6G," *IEEE Commun. Surv. Tutorials*, vol. 26, no. 3, pp. 1478–1519, 2024.
- [10] J. Zhang, J. Lin, P. Tang, W. Fan, Z. Yuan, X. Liu, H. Xu, Y. Lyu, L. Tian, and P. Zhang, "Deterministic Ray Tracing: A Promising Approach to THz Channel Modeling in 6G Deployment Scenarios," *IEEE Commun. Mag.*, vol. 62, no. 2, pp. 48–54, 2024.
- [11] Z. Yuan, J. Zhang, V. Degli-Esposti, Y. Zhang, and W. Fan, "Efficient Ray-tracing Simulation for Near-field Spatial Non-stationary mmWave Massive MIMO Channel and Its Experimental Validation," *IEEE Trans. on Wireless Commun.*, vol. 23, no. 8, pp. 8910–8923, 2024.
- [12] Y. Chen, Y. Li, C. Han, Z. Yu, and G. Wang, "Channel Measurement and Ray-Tracing-Statistical Hybrid Modeling for Low-Terahertz Indoor Communications," *IEEE Trans. Wireless Commun.*, vol. 20, no. 12, pp. 8163–8176, 2021.
- [13] Y. Zeng and X. Xu, "Toward Environment-Aware 6G Communications via Channel Knowledge Map," *IEEE Wireless Commun.*, pp. 84–91, Jun 2021.
- [14] C. De Lima, D. Belot, R. Berkvens, A. Bourdoux, D. Dardari, M. Guillaud, M. Isomursu, E.-S. Lohan, Y. Miao, A. N. Barreto *et al.*, "Convergent Communication, Sensing and Localization in 6G Systems: An Overview of Technologies, Opportunities and Challenges," *IEEE Access*, vol. 9, pp. 26902–26925, 2021.
- [15] S. Zhang, A. Wijesinghe, and Z. Ding, "RME-GAN: A Learning Framework for Radio Map Estimation Based on Conditional Generative Adversarial Network," *IEEE Internet Things J.*, vol. 10, no. 20, pp. 18016–18027, 2023.
- [16] X. Li, S. Zhang, H. Li, X. Li, L. Xu, H. Xu, H. Mei, G. Zhu, N. Qi, and M. Xiao, "RadioGAT: A Joint Model-Based and Data-Driven Framework for Multi-Band Radiomap Reconstruction via Graph Attention Networks," *IEEE Trans. Wireless Commun.*, vol. 23, no. 11, pp. 17777–17792, 2024.
- [17] D. Minovski, N. Ögren, K. Mitra, and C. Åhlund, "Throughput Prediction Using Machine Learning in LTE and 5G Networks," *IEEE Trans. Mob. Comput.*, vol. 22, no. 3, pp. 1825–1840, 2021.
- [18] S. Li, E. Magli, G. Francini, and G. Ghinamo, "Deep learning based prediction of traffic peaks in mobile networks," *Computer Networks*, vol. 240, p. 110167, 2024.
- [19] A. Al-Thaedan, Z. Shakir, A. Y. Mjhoor, R. Alsabah, A. Al-Sabbagh, F. Nembhard, and M. Salah, "A machine learning framework for predicting downlink throughput in 4g-LTE/5G cellular networks," *International Journal of Information Technology*, vol. 16, no. 2, pp. 651–657, 2024.
- [20] M. Bernabè, D. López-Pérez, N. Piovesan, G. Geraci, and D. Gesbert, "Massive MIMO for Aerial Highways: Enhancing Cell Selection via SSB Beams Optimization," *IEEE Open J. Commun. Soc.*, vol. 5, pp. 3975–3996, 2024.
- [21] J. Wang, Q. Zhu, Z. Lin, Q. Wu, Y. Huang, X. Cai, W. Zhong, and Y. Zhao, "Sparse Bayesian Learning-Based 3-D Radio Environment Map Construction—Sampling Optimization, Scenario-Dependent Dictionary Construction, and Sparse Recovery," *IEEE Trans. Cognit. Commun. Networking*, vol. 10, no. 1, pp. 80–93, 2024.
- [22] J. Wang, Q. Zhu, Z. Lin, J. Chen, G. Ding, Q. Wu, G. Gu, and Q. Gao, "Sparse Bayesian Learning-Based Hierarchical Construction for 3D Radio Environment Maps Incorporating Channel Shadowing," *IEEE Trans. Wireless Commun.*, vol. 23, no. 10, pp. 14560–14574, 2024.
- [23] J. Lyu and R. Zhang, "Network-Connected UAV: 3-D System Modeling and Coverage Performance Analysis," *IEEE Internet Things J.*, vol. 6, no. 4, pp. 7048–7060, 2019.
- [24] C. K. Armeniakos and A. G. Kanatas, "Performance Comparison of Wireless Aerial 3D Cellular Network Models," *IEEE Commun. Lett.*, vol. 26, no. 8, pp. 1779–1783, 2022.
- [25] S. J. Maeng and I. Güvenç, "UAV Corridor Coverage Analysis With Base Station Antenna Uplift and Strongest Signal Association," *IEEE Trans. Aerosp. Electron. Syst.*, vol. 60, no. 4, pp. 5621–5630, 2024.
- [26] S. Zhang, X. Ning, X. Zheng, Q. Shi, T.-H. Chang, and Z.-Q. Luo, "A Physics-Based and Data-Driven Approach for Localized Statistical Channel Modeling," *IEEE Trans. Wireless Commun.*, vol. 23, no. 6, pp. 5409–5424, 2024.
- [27] W. He, C. Zhang, Y. Huang, and X. You, "Intelligent Optimization of Base Station Array Orientations via Scenario-Specific Modeling," *IEEE Trans. Commun.*, vol. 70, no. 3, pp. 2117–2130, 2021.
- [28] X. Gao, X. Zhu, and L. Zhai, "AoI-Sensitive Data Collection in Multi-UAV-Assisted Wireless Sensor Networks," *IEEE Trans. Wireless Commun.*, vol. 22, no. 8, pp. 5185–5197, 2023.
- [29] X. Wang, H. Chen, S. Tang, Z. Wu, and W. Zhu, "Disentangled Representation Learning," *IEEE Trans. Pattern Anal. Machine Intell.*, vol. 46, no. 12, pp. 9677–9696, 2024.
- [30] N. Moraitis, K. Psychogios, and A. D. Panagopoulos, "A Survey of Path Loss Prediction and Channel Models for Unmanned Aerial Systems for System-Level Simulations," *Sensors*, vol. 23, no. 10, 2023.
- [31] Y. Teganya and D. Romero, "Deep Completion Autoencoders for Radio Map Estimation," *IEEE Trans. Wireless Commun.*, vol. 21, no. 3, pp. 1710–1724, 2022.
- [32] N. Srivastava, G. Hinton, A. Krizhevsky, I. Sutskever, and R. Salakhutdinov, "Dropout: a simple way to prevent neural networks from overfitting," *J. Mach. Learn. Res.*, vol. 15, no. 1, p. 1929–1958, Jan. 2014.
- [33] H. Wang, Y. Huang, R. Gao, and F. Calmon, "Analyzing the Generalization Capability of SGLD Using Properties of Gaussian Channels," in *Advances in Neural Information Processing Systems*, M. Ranzato, A. Beygelzimer, Y. Dauphin, P. Liang, and J. W. Vaughan, Eds., vol. 34. Curran Associates, Inc., Dec. 2021, pp. 24222–24234.
- [34] A. Xu and M. Raginsky, "Information-theoretic analysis of generalization capability of learning algorithms," in *Proceedings of the 31st International Conference on Neural Information Processing Systems*. Red Hook, NY, USA: Curran Associates Inc., Dec. 2017, p. 2521–2530.
- [35] L. Eller, P. Svoboda, and M. Rupp, "A Deep Learning Network Planner: Propagation Modeling Using Real-World Measurements and a 3D City Model," *IEEE Access*, pp. 122182–122196, Jan 2022.
- [36] S. Mohammadjafari, S. Roginsky, E. Kavurmacioglu, M. Cevik, J. Ethier, and A. B. Bener, "Machine Learning-Based Radio Coverage Prediction in Urban Environments," *IEEE Trans. Netw. Serv. Manag.*, vol. 17, no. 4, pp. 2117–2130, 2020.
- [37] C. E. G. Moreta, M. R. C. Acosta, and I. Koo, "Prediction of Digital Terrestrial Television Coverage Using Machine Learning Regression," *IEEE Trans. Broadcast.*, vol. 65, no. 4, pp. 702–712, 2019.
- [38] R. He, Y. Gong, W. Bai, Y. Li, and X. Wang, "Random Forests Based Path Loss Prediction in Mobile Communication Systems," in *Proc. IEEE Int. Conf. Comput. and Commun. (ICCC)*, Chengdu, China, Dec. 2020, pp. 1246–1250.
- [39] X. Wang and Q. Zhou, "LTE Network Quality Analysis Method Based on MR Data and XGBoost Algorithm," in *Proc. IEEE Int. Conf. Big Data Analytics (ICBDA)*, Xiamen, China, May 2020, pp. 85–89.